Title
A Preliminary Calibration of Radial Neutron Time-Of-Flight Detectors on a Dense Plasma Focus

Author
Vaughan, Jacquelynne

Publication Date
2022

Peer reviewed|Thesis/dissertation

UNIVERSITY OF CALIFORNIA SAN DIEGO

A Preliminary Calibration of Radial Neutron Time-Of-Flight Detectors on a Dense Plasma Focus

A Thesis submitted in partial satisfaction of the requirements

for the degree Master of Science

in

Mechanical and Aerospace Engineering

by

Jacquelynne deValcourt Vaughan

Committee in charge:

Professor Farhat Beg, Chair
Professor Alexey Arefiev
Professor Nicholas Boechler

2022

The Thesis of Jacquelynne deValcourt Vaughan is approved, and it is acceptable in quality and form for publication on microfilm and electronically.

University of California San Diego

2022

DEDICATION

For my Aunt Gina, Grandpa Bill, and Grandma Delores.

Table of Contents

THESIS APPROVAL PAGE……...iii
DEDICATION iv
LIST OF FIGURES vi
LIST OF TABLES vii
LIST OF SYMBOLS viii
ACKNOWLEDGEMENTS ix
ABSTRACT OF THE THESIS xi
INTRODUCTION 1
Plasmas and Nuclear Fusion 1
The Dense Plasma Focus 3
Neutron Detection on a DPF 5
EXPERIMENTAL DESIGN AND METHODS 7
The 4.6-kJ DPF and Diagnostics 7
Beryllium Activation Detector 9
Neutron Time-Of-Flight 10
Proton Recoil 10
Photomultiplier Tubes 10
X-Ray Shielding 12
Solid Angle 12
nTOF Signal Area 13
RESULTS AND ANALYSIS 15
Signal Analysis Method 15
Cross Calibration of the Top and Bottom nTOFs 17
Calibrating nTOF Signal Area to Neutron Yield 18
DISCUSSION AND FUTURE WORK 22
REFERENCES 24

LIST OF FIGURES

Figure 1: A figure illustrating the different regions of high energy density physics phenomena, outlined by different pressure hugoniot traces, taken from the NRC report, *Frontiers in High Energy Density Science*.....2

Figure 2: The main phases of a DPF implosion, illustrated.....3

Figure 3: A Schlieren image of a plasma mushrooming out of the top of the cathode-anode coaxial tunnel.....4

Figure 4: Figure taken from [7] demonstrating the anisotropy of beam target versus thermonuclear fusion-generated neutrons.....5

Figure 5: A schematic of the DPF electrodes and a photograph of the DPF exterior in the lab……..7

Figure 6: Example diagnostic traces of dI/dt, X-ray PIN diode, and the two radial nTOF detectors.....8

Figure 7: Illustrated Be-activation bin counts, decay, and photo inset of lab set-up.....9

Figure 8: An example schematic of a scintillator and photomultiplier tube as a neutron time-of-flight detector.....11

Figure 9: An example nTOF trace.....14

Figure 10: An original nTOF signal and a smoothed version of that signal.....16

Figure 11: Two example plots of nTOF traces from the Top and Bottom nTOF detectors exhibiting both shielding and no shielding.....17

Figure 12: A scatter plot of the cross-calibration fit…..…….....17

Figure 13: Scatter plot of nTOF neutron areas versus neutron number count at detector solid angle.....18

Figure 14: nTOF pulse width histogram distributions…….....19

Figure 15: Scatter plot of the areas versus neutron flux distinguished by oscilloscope and Top and Bottom……..……20

LIST OF TABLES

Table 1. EJ-204 and Hamamatsu R7724 detector parameters……..…….…….....12

Table 2. Fit data for the Top and Bottom nTOF detectors by neutron flux and area…….….....18

LIST OF SYMBOLS

p	proton
n	neutron
H	hydrogen
He	Helium
D	^{2}H or deuterium
T	^{3}H or tritium
Be	Beryllium
e	electron charge ($1.602 \cdot 10^{-19}$ C)
q	particle charge
m	neutron mass ($1.675 \cdot 10^{-24}$ kg)
E	energy
V	Volts
DD	nomenclature referring to a deuterium-deuterium nuclear fusion reaction
DT	nomenclature referring to a deuterium-tritium nuclear fusion reaction
PMT	photomultiplier tube
nTOF	neutron time-of-flight
ns	nanoseconds
ps	picoseconds
kV	kilovolts
J	Joules
MJ	Megajoules

ACKNOWLEDGEMENTS

Drs. Troy Carter (UCLA), Scott Hsu (LANL/DOE), and Verena Geppert-Kleinrath (LANL) gave me my first opportunities to do real physics research. Though I struggled at times, they all supported me.

Thank you to Dr. Quinn Looker (SNL) for his patience and guidance. Dr. Mathieu Bailly-Grandvaux (UCSD) always gave a great pep talk that managed to re-motivate me and bring my spirits up. Quarantine was hard, y'all. Many thanks also go to Drs. Fabio Conti and Pia Valdivia. The former for providing expertise on neutron detectors and providing feedback on various experimental steps, and to Dr. Valdivia for feedback too, as well as for kicking me into gear when I needed it. They are wonderful mentors and teachers. I'd also like to thank my advisor, Dr. Farhat Beg, for providing me this opportunity to write this thesis for a Masters.

I had so many peers who guided, mentored, and comforted me along the way: (in no particular order, not including everyone, and for title's sake, mostly Drs. or soon-to-be) R. Roycroft, J. Strehlow, K. Weichman, S. Miller, M. Adams, K. Bhutwala, B. Pagano, C. Harris, SJ Spencer, E. Takasugi, A. Raymer, J. Fromm, J. Lynch, L. Matsunobu, D. Schaper, J. Pilgram, and H.R. Hasson. Many thanks to my lab mate, Veronica Eudave – someday I'll be bragging to my friends that I worked with the JPL director! #sunglassesemoji #manifesting

To my friends and family: Thomas Murray ("the one and only"), Ashoka Thalia (waow), Karandeep Singh, Lizzi Vaughan, David Vaughan, Shelby Brown, my niblings, my Dad, my Mom, and many others. I am grateful you are my community, and for the support and love I receive as I trek random roads and trip over potholes.

To the Plasma Gods I give this thesis; to the Electronics Deities my confusion; to the Caen Sales Rep Guy (Greg Kibilko), a big thank you; and to the Spot, which gave me my first community in San Diego, a big hug.

The money comes from somewhere: this work was funded by the DOE grant, DE-NA0003842.

ABSTRACT OF THE THESIS

A Preliminary Calibration of Radial Neutron Time-Of-Flight Detectors on a Dense Plasma Focus

by

Jacquelynne deValcourt Vaughan

Master of Science in Mechanical and Aerospace Engineering

University of California San Diego, 2022

Professor Farhat Beg, Chair

Neutron time-of-flight (nTOF) detectors are commonly used for fast neutron detection on nuclear fusion plasma experiments in high energy density physics. The 4.6-kJ dense plasma focus (DPF) at UC San Diego can generate neutron yields of up to ~10^8. Two nTOF detectors radially situated at 1.3 m from the DPF are each composed of an EJ-204 plastic scintillator and an Hamamatsu R7724 photomultiplier tube. Several hundred experimental shots have been taken

over the course of four different anode types. Of those, 203 shots with neutron data were selected to calibrate both nTOF detectors. A Be-activation detector generates absolute neutron yield data and has a lower detection limit of $1.1 \cdot 10^6$ neutrons. The latter is used to calibrate the signal areas in the nTOF data, and directly correlate those signal areas with the number of neutrons incident on the detector at its radius from the DPF. This preliminary analysis finds that the two nTOF detectors have approximate efficiencies of 8100 and 1700 photons per DD neutron, respectively. Further analysis can improve the correlation as well as investigate the cross-calibration between the two nTOF detectors more thoroughly.

INTRODUCTION

Plasmas and Nuclear Fusion

Plasmas make up over 99% of visible matter in the universe, namely, in the form of stars. They also partially compose interstellar medium, and even parts of planetary atmospheres. As our solar system treks its path in the Milky Way, it forms a coronal plasma that defines its edges that make contact with the surrounding space.

Even if plasma physicists fight over the details of what a plasma is or can be, they can typically agree on a few features that distinguish it as its own phase of matter from gasses, solids, and others. For the layperson, we typically will start with: “a hot, ionized gas.” After all, heating a gas can turn it into a plasma. But, not all hot ionized gasses are plasmas. For instance, unlike neutral gasses, “quasineutral” plasmas behave collectively in response to introduced electromagnetic charges. Additionally, a plasma’s density is large enough that this collective behavior of their constituent particles arises; and their energy/temperature is large enough that any introduced charges or fields does not dissipate the plasma from its original form [1]. Nicholson [2] reframes that last point, noting that individual particles in the plasma should have much more energy than the potential energy induced in them by neighboring particles.

Within “high energy density physics” (HEDP) we concern ourselves with plasmas that are very hot, very dense, and very energetic – usually we consider plasmas at 1Mbar pressure as those that are within the realm of HEDP (1 Mbar specifically corresponds to the energy it takes to ionize a Hydrogen atom).

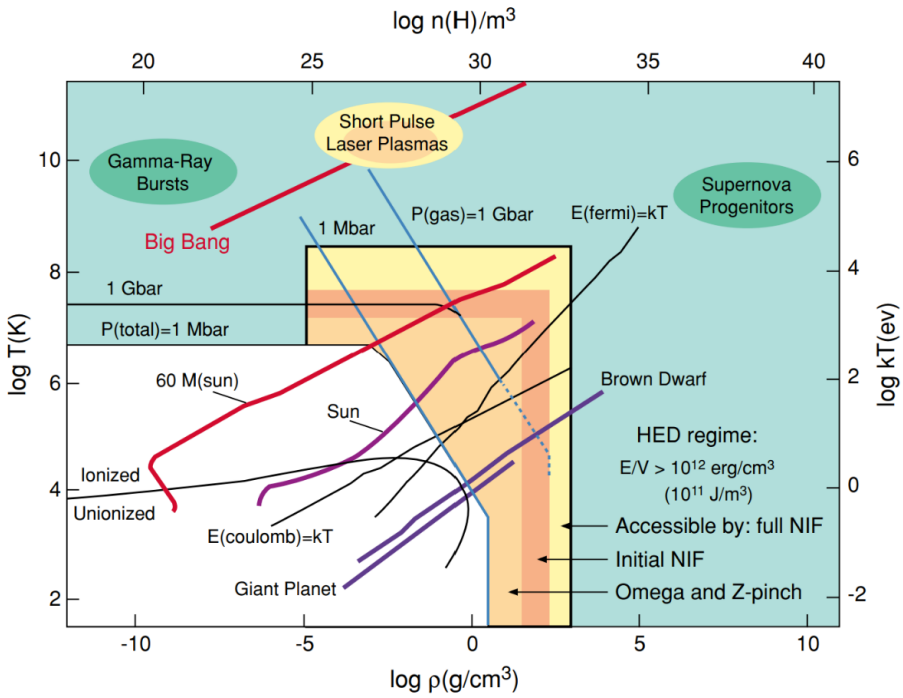

Figure 1. A figure illustrating the different regions of high energy density physics phenomena, outlined by different pressure hugoniot traces, taken from the NRC report, *Frontiers in High Energy Density Science*. [3] 1 Mbar is the standard for what plasmas are considered to be in the high energy density regime.

The inception of this field began with the development of the atomic bomb, and in the United States has grown to research at universities and notably, national laboratories that formed from the Manhattan Project. More familiarly, the field is the nexus of nuclear fusion and plasma.

In practice, nuclear fusion is an exothermic reaction between two or more hydrogen isotopes (i.e. deuterium, tritium) that releases the combined energy into X-rays, neutrons, and depending on the original particles fusing, different isotopes of Helium.

$$D + D \rightarrow {}^{3}He(0.8\ MeV) + n(2.45\ MeV) \qquad (1)$$

A DD reaction is one commonly implemented nuclear fusion reaction implemented in HEDP experiments, where two deuterium isotopes fuse and generate Helium-3's and 2.45 MeV neutrons. [1] The work in this thesis studies neutron products of DD reactions within a Dense Plasma Focus (DPF).

The Dense Plasma Focus

Within HEDP there are several ways to induce nuclear fusion in plasmas. Those techniques are encapsulated within different categories of fusion, like ICF (inertial confinement fusion, wherein an external force confines a plasma to fusion conditions), MCF (magnetic confinement fusion, where strong magnetic fields confine a plasma to fusion conditions), and hybrids of ICF and MCF. Variations of those hybrids include systems that use pulsed power to inject an energetic electric pulse into a gas, inducing Lorentz forces in the subsequent plasma that causes the plasma to implode to fusion conditions. These implosions are commonly Z-pinches, where an axial current self-generates a magnetic field, and the resulting JxB force causes the plasma to radially implode and compress to fusion-like conditions.

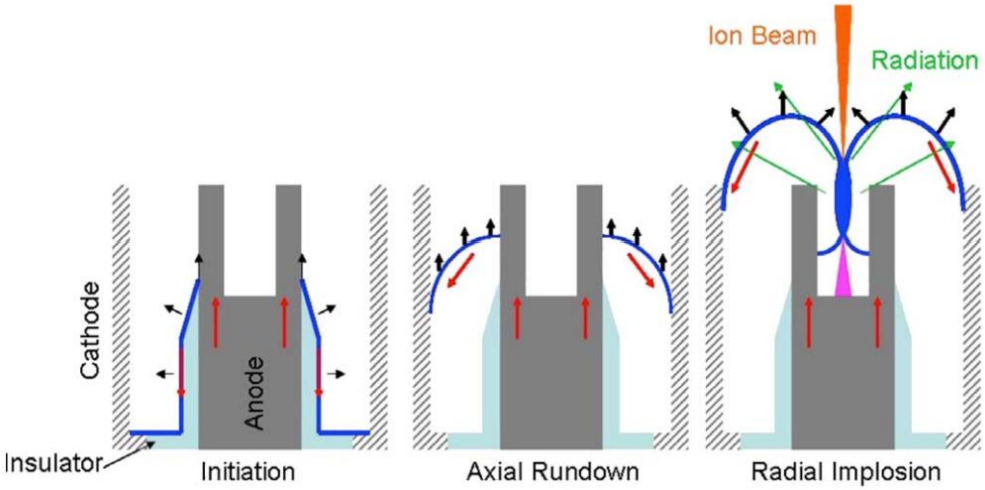

Figure 2. A figure from Krishnan [4] showing the main phases of a DPF implosion. At initiation, a thin gas formed from insulator material becomes a plasma sheath that travels down the cathode and anode, ending in radial implosion wherein the mushrooming plasma coalesces into a column at the tip of the anode, forming into a pinch. The blue line indicates the plasma sheath, the green arrows indicate the photon radiation, and the orange arrow the ion beam that subsequently forms.

The field of "pulsed power" systems includes the dense plasma focus (DPF). The DPF is a coaxial configuration of an anode and cathode, with a source of plasma material (an "insulator sleeve") at the base of the anode. The cathode rods are concentric with the anode. A capacitor

stores the energy, usually on the order of kJ or MJ, which is discharged upon the release of a switch in the circuit.

This discharge initiates the formation of a plasma sheath over the insulator sleeve. The current that passes radially across the electrodes, *J*, self-generates an azimuthal magnetic field, *B*, and the resulting axial JxB force propels the plasma sheath down the gap between the anode and electrode to an open end. As the sheath exits the gap, it begins to "mushroom out" and the axial JxB force converts into an inward radial JxB force that results in a Z-pinch as the current (J) becomes axial. The pinch releases X-rays and other forms of radiation, like neutrons, depending on the material and gas used to create the plasma. Figure 2 [4] illustrates the three main stages of the DPF. DPF research began in the 1960's and was independently invented by various groups [5] [6]. At UC San Diego, the Center for Matter under Extreme Conditions (CMEC) hosts a 4.6-kJ Mather-style DPF capable of 10^8 neutron yields [13].

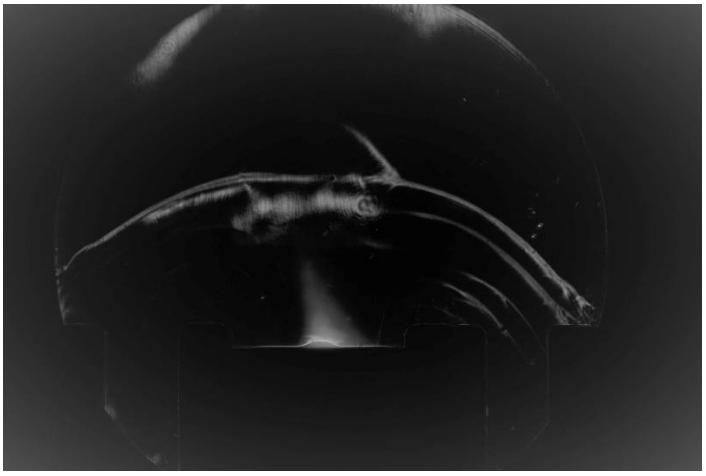

Figure 3. A Schlieren image of a plasma mushrooming out of the top of the cathode-anode coaxial tunnel.

Recent research [15] at UC San Diego on different anode configurations and insulator sleeve lengths illustrate how neutron and hard X-ray yields vary when the DPF components are modified. Henceforth this thesis will focus on the methods used to determine the neutron yield of

the DPF over these various configurations, and on calibrating the neutron detectors used to supplement this yield data.

Neutron Detection on a DPF

Neutron detection on a DPF can illuminate how exactly the DPF creates those neutrons. Beam-target (BT) fusion and thermonuclear (TN) fusion are two processes that can generate those neutrons (given an appropriate fill gas in the chamber, such as deuterium). Studies indicate that an anisotropy in the angular distribution of this neutron emission would reveal how much of that neutron creation is BT versus TN fusion [7].

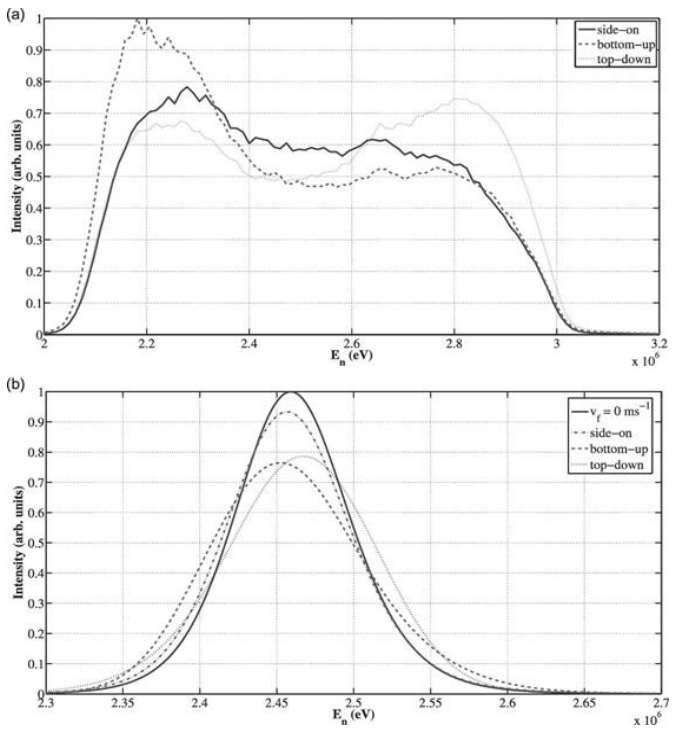

Figure 4. Figure taken from [7]. Top: beam-target fusion neutron spectra off a 2-MA DPF from axial and radial directions. Bottom: the same, but for thermonuclear fusion spectra.

Calibrating nTOF detectors would allow for placing them at different angles (i.e. radially versus axially) with respect to the DPF source to study this anisotropy. Furthermore, given whatever lower yield limit another neutron detector may have (like an activation detector –

described in the next chapter), calibrating nTOF detectors could extend this lower sensitivity and allow for measuring even lower yields when the latter detector cannot. Thus, the work in this thesis starts a preliminary calibration of two nTOF detectors for the purposes described.

Because a neutron has zero electric charge, neutron detectors actually take advantage of its high likelihood of scattering with a variety of elements. The products of collisions between neutrons and various atoms are measured in various ways instead of directly observing the neutrons. Of these methods, two main classes of detectors exist: activation [11], and neutron time-of-flight (nTOF). This thesis is a calibration of nTOF detectors.

Activation detectors count the quantums of collisional products from neutrons impinging on various elemental isotopes, whose decay products are converted into signal. Thus, an absolute neutron yield can be measured. Neutron time-of-flight detectors utilize the distance of the detector from the source of neutrons to generate energy spectra based on the neutrons' velocities and thus times of arrival at the detector.

EXPERIMENTAL DESIGN AND METHODS

The 4.6-kJ DPF and Diagnostics

Over the course of collecting this data, four different anodes were used in the DPF at a given time. Those four anodes are: the hemispherical hollow anode; the hemispherical solid anode; a flat slit anode; and a flat hollow anode. Research has shown that different anode types change the X-ray and neutron yields [13] [15]. For this analysis, because we are correlating neutron yield with nTOF signal area, anode type will not factor into the calculations other than that some anodes produce more neutrons than others.

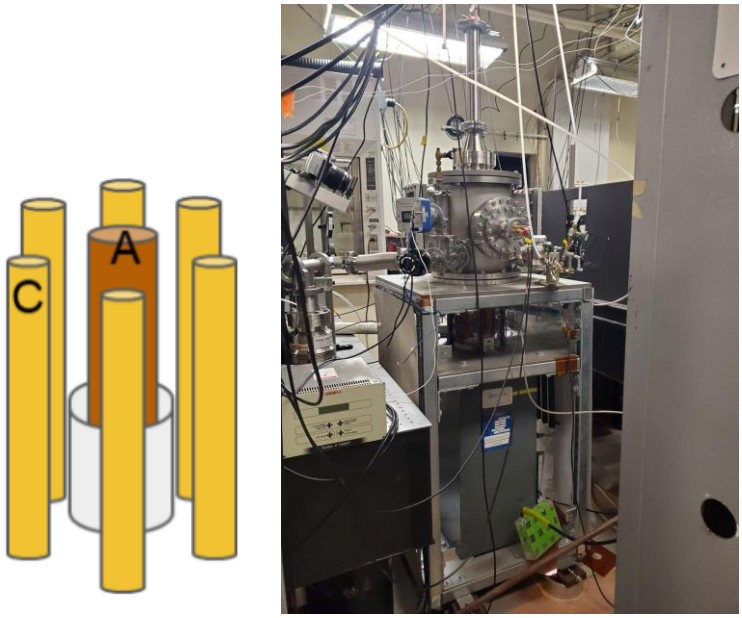

Figure 5. Left: a simple schematic of the anode and cathode rods that encircle it. The yellow cylinders represent the cathode rods, and the central brown cylinder the anode. The gray cylinder at the base of the anode illustrates the insulator sleeve. Right: a photograph taken of the exterior of the DPF. A vacuum chamber encloses the anode and cathode rods. A capacitor sits below the chamber, and various piping and cables surround the entire set-up.

Several different diagnostics are fielded on the DPF, but this analysis will only focus on neutron time-of-flight detectors. These include: the differential of the current in time (dI/dt), a voltage measured off a Rogowski coil probe; and the Top and Bottom nTOFs. A top Aluminum

PIN diode was implemented to verify that pinch timing generally coincides with the X-ray signal rise time on the diode (Figure 6). Cable length delays for all diagnostics are included in the time vectors for the different diagnostics' data.

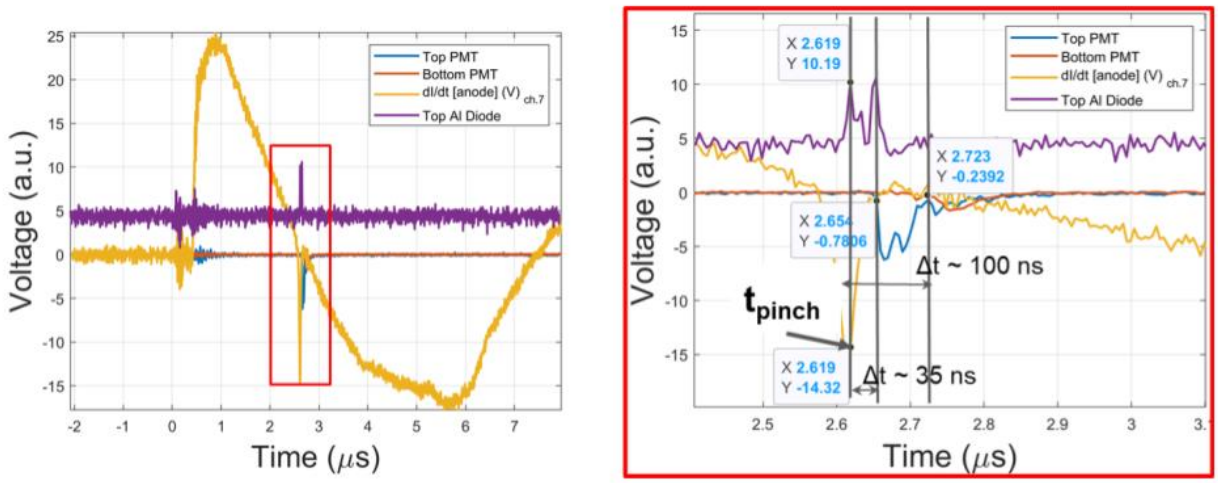

Figure 6. Example traces from different diagnostics on the UCSD DPF. The yellow trace is the dI/dt signal measured off the Rogowski coil. The purple is an X-ray PIN diode trace. The blue and red traces are the Top and Bottom nTOF signals, respectively. Right: a zoomed-in section of the figure from the left highlights the timing differences between different peak formations in the diagnostics. The first X-ray peak coincides with the discontinuity in the dI/dt trace.

The Top and Bottom nTOF detector signals were nominally evenly voltage divided between two oscilloscopes named SPOCK (200 MS/s) and LEIA (1 GS/s), and no signal was attenuated.

As can be seen in Figure 6, the nTOF trace in blue (corresponding to the Top nTOF) shows an initial response in time within about 35-40 nanoseconds after the discontinuity peak time in the dI/dt trace, as well as the two X-ray peaks seen in the PIN diode trace (purple). Because DD neutrons would not arrive at the detector until about 60 ns after the pinch peak, and an additional 30 ns would delay the neutron signal from arriving at an oscilloscope, this response seen in the nTOF trace would very likely not correspond to neutrons. At minimum it would include X-rays. The handling of this timing is discussed in the Results and Analysis chapter.

Beryllium Activation Detector

A Beryllium activation detector from Mission Support and Test Services provides absolute neutron yield data for DPF experiments at UC San Diego. It was calibrated to a continuous single neutron source at the Ion Beam Laboratory at Sandia National Laboratory in Albuquerque, NM. The absolute yield data from this detector will be used to directly calibrate the two nTOF detectors in this thesis.

The Be-activation detector generates an end product of electrons which are counted into 160 ms time-separated bins, and integrated over 8 total seconds to capture the decay and account for noise. These electron products are created through the beta decay of Helium-6 into Lithium-6, which has an 806 ms-halflife. The He-6 are generated from the alpha decay of Be-9, induced by a neutron impact. Thus, the end number of electrons directly corresponds to the number of neutrons that impacted the Be-9 in the detector. The electrons are collected with a PMT biased at -2.2 kV, and are separated into bins by a 15 mV constant fraction discrimination signal threshold.

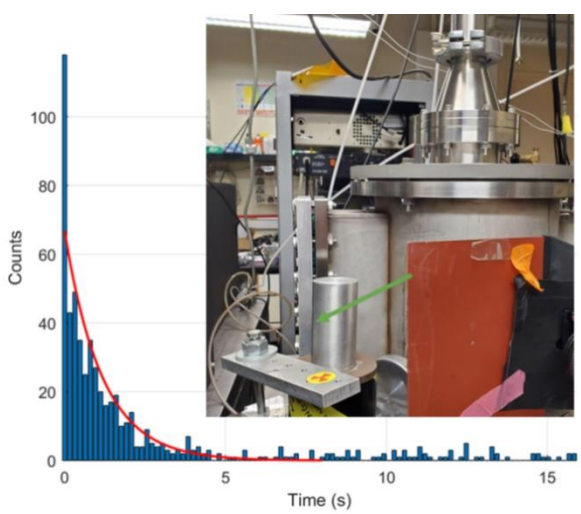

Figure 7. The inset is a photo of the Be-activation detector next to the DPF source. The green arrow denotes the direction of neutron impact on the detector. The graph is a data set of bin counts generated by the detector. The red dashed line indicates the decay, implying this particular set of counts detected a neutron yield above the lower threshold limit of $1.1 \cdot 10^6$.

Neutron Time-Of-Flight

nTOF detectors can generate neutron energy spectra if a detector is placed at a distance from the neutron source such that neutrons of different energies, and hence velocities, will arrive at the detector at different times. The distance of the detector will determine when those neutrons arrive as well as the energy resolution (closer distances will have narrower energy spreads). For a DD neutron (2.45 MeV), and an nTOF placed at 1.3 meters, that neutron will reach the nTOF at ~60 ns from generation time in the plasma source.

$$TOF(ns) = 10^6 \cdot R \cdot \sqrt{\frac{2e}{m} \cdot E} \qquad (4)$$

where *TOF* is the time-of-flight in nanoseconds; *R* is the distance from DPF source to detector; and *E* is the neutron energy in MeV. The prefactor comes from the unit conversion to nanoseconds and from MeV to Joules.

Proton Recoil. A scintillator at the front of the nTOF detector convert the neutrons to visible light. Proton recoil by neutron impact, or n-p elastic scattering, is the main scintillating process in plastic scintillators used for fast neutron detection [9] [12]. When a neutron impinges on a lattice composed with a significant amount of Hydrogen atoms, a proton "recoil" generates visible photons. In total, this whole process is known as scintillation. A quantum of radiation - in this case, a neutron - impacts a material which converts that radiation into visible light.

Photomultiplier Tubes. One needs to either count these scintillating photons directly or convert them into a signal. In the case of most nTOF detectors, photomultiplier tubes convert the scintillation light into a voltage. A photocathode at the front of the PMT converts photons into electrons via the photoelectric effect. Then, the initial bunch of electrons formed accelerate to a

“dynode,” a negatively biased electrode. The electrons impinge on this plate, knocking out more electrons within it. The initial electron number, now amplified by the new electrons created from the collisions in the first dynode, accelerate to a consecutive dynode at a more negative voltage. This process repeats itself until a final group of electrons accelerates to a final anode. The amplification of the initial number of electrons can be on the order of ~10^6. Also, this process takes time, typically called the “transit time”, and can be on the order of several tens of nanoseconds.

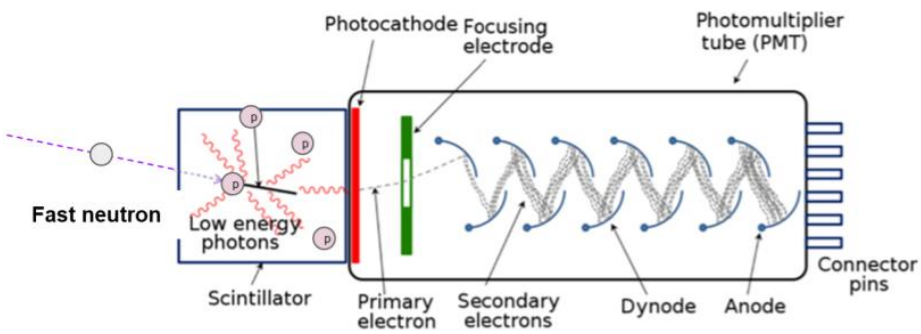

Figure 8. A simplified example schematic of a photomultiplier tube in junction with a scintillator. Little circles denoted with “p” represent recoiling protons. A photocathode at the front of the PMT converts scintillating “low energy” photons into electrons, which are directed to the first dynode by a focusing electrode. The subsequent multiplication over the course of the rest of the dynodes, to the final anode, is illustrated. [8]

The type of PMT used for both nTOFs is a Hamamatsu 7724. Its properties are listed in Table 1. The quantum efficiency of the photocathode is the percentage conversion of photons to electrons. The gain is the amount by which the initial number of electrons increase from the photocathode by the time they reach the anode. The transit time spread is how much the electron signal widens over the course of the amplification across all dynodes, and the transit time is how long the amplification process takes. Table 1 lists the various parameters for the scintillator and PMT that compose each nTOF detector calibrated in this thesis.

Table 1. A table of properties for the EJ-204 scintillator and the Hamamatsu R7724 PMT.

Parameter	EJ-204	Hamamatsu R7724
Rise time (ns)	0.7	2.1
Decay time || Transit time (ns)	1.8	29
Pulse width || Transit time spread (ns)	2.2	1.2
Efficiency (scintillation || quantum – photocathode)	10,400 photons/1 MeV e^-	26%
Gain	/	$3.3 \cdot 10^6$

X-Ray Shielding. The generation of fast neutrons in a plasma typically coincides with the generation of X-rays, since both are products of nuclear fusion reactions. nTOFs are also sensitive to X-rays as well as neutrons, so care must be taken if one wants to distinguish between the two. Shielding with a high-Z material can block a large part of the X-ray spectrum generated in an experiment. A lead (Pb) puck was placed in front of the "Bottom nTOF" for the shot data collected for this thesis.

Having an additional detector that can relay the X-ray timing in an experiment will help to identify the timing region of X-rays in an nTOF output signal. A second PMT nTOF, the "Top nTOF", was unshielded for the collection of the data in this thesis. A cross-calibration later discussed was performed for some shots where the Pb shielding was removed for the Bottom nTOF.

Solid Angle. In order to correlate any absolute yield information from the activation detector with the nTOF signals, the detector "solid angle" must also be taken into account. This parameter is the ratio of the active detection area on the detector (the surface area on the detector face that

actively collects radiation and translates it into signal) to the total spherical area with a radius equal to the distance of the detector from the neutron source. In this case, the diameter of the active detection area of one nTOF is 2”, and the distance 1.3 m. This ratio determines the fraction of the radiation yield that will reach the detector. Dependent on the sensitivity and efficiency of that detector, a fraction of the radiation will translate into signal.

nTOF Signal Area. Finally, we see how the signal from an nTOF detector can be used to extract information about the neutrons generated in an experiment by a plasma or fusion source. Given the photoconversion efficiency and gain of a Hamamatsu R7724 PMT, a rough total efficiency of an nTOF detector can be calculated using the areas of waveforms detected and give approximate light yields for the EJ-204 scintillators used.

A typical nTOF signal looks like such as in Figure 9. It is voltage traced in time, and if one integrates the area it gives Coulombs. This number of Coulombs can be translated into a number of electrons. Factoring out the gain from the PMT and its photocathode efficiency gives the initial number of scintillation photons that originally impinged on the photocathode. Thus, one can estimate the light yield of a single DD neutron.

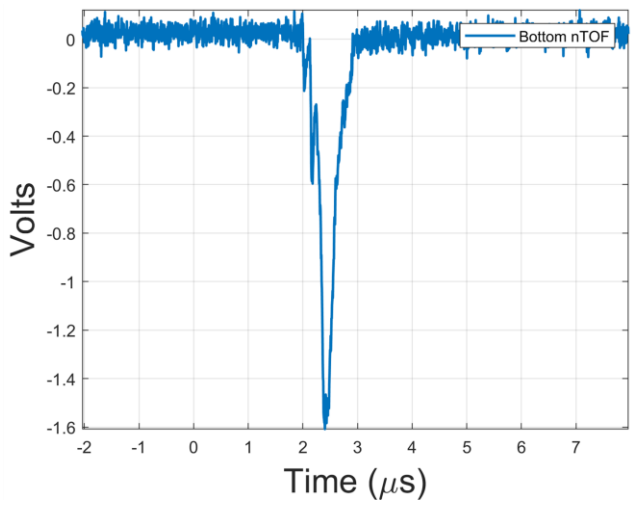

Figure 9. An example trace of a neutron time-of-flight signal from a detector with a negative bias on the PMT. The shorter spikes on the "rising" edge of the peak are likely from X-rays.

To improve the accuracy of this calculation, one can also take into account the rise and decay times of the scintillator and PMT. These all contribute to the time width of nTOF waveforms. In this analysis this constant width is included in the waveform areas calculated, so the calculated photon yields per DD neutron will be overestimates that will need to be determined in further analysis not in this thesis.

RESULTS AND ANALYSIS

Signal Analysis Method

A total of 203 shots over all four anodes were selected for analysis. Those removed include: waveforms with low signal-to-noise ratio (SNR); low SNR signals with double peaks; and empty data sets. For a given nTOF waveform, cable length delay was subtracted from the signal's corresponding time vector/window. Then, the mean of the base signal (before any neutron or X-ray signal presented itself in the time window) was subtracted from the total signal, eliminating background contribution to voltage amplitude.

Next, the data was smoothed with a Savitzky-Golay (SG) filter of order 2 and window 11. The SG filter uses a low-order polynomial to fit data points over a given window, unlike, say using a moving average filter that only takes the average of all the given points within a window and applying that value to the centroid. Then, the SG filter can have less effect on signal shape. A polynomial of order 2 with a window length of 11 (i.e. corresponding to 11 ns resolution in the LEIA data sets) was chosen after testing the SG filter with different orders and window lengths to determine which performed the best. The length of the window did not appear to have an effect on the signal response in time. Figure 9 shows an example of a noisy nTOF signal compared with an SG-smoothed version of that signal.

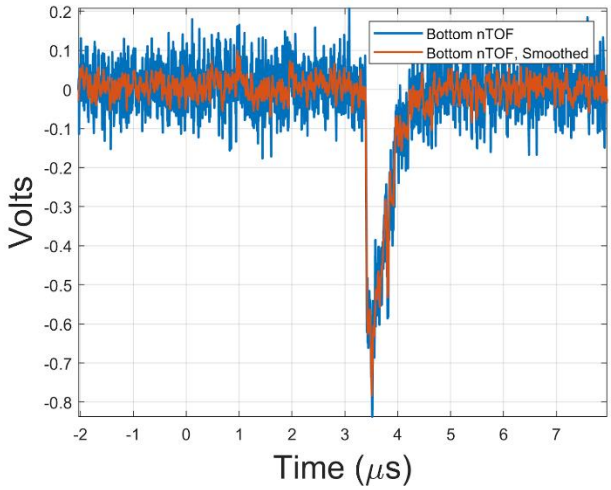

Figure 10. An example trace of an original Bottom nTOF trace, and a Bottom nTOF trace smoothed with a Savitzky-Golay filter of order 2 and window length 11.

Meanwhile, the pinch peak in the dI/dt data is found by using MATLAB's islocalmin() and identifying the peak with the largest prominence, after smoothing the dI/dt data with the same Savitzky-Golay filter. The corresponding time the peak occurs in the data is stored for comparison with the nTOF signals. Because every shot always had a dI/dt trace, but not every shot had an X-ray diode trace, dI/dt was used for determining possible X-ray timing that could occur in a given shot.

Finally, the peak time found in the dI/dt data is then translated to nTOF time windows by aligning the t=0 of the dI/dt and nTOF time windows. Subsequently, a search using find() picks the first time point following pinch time (tp), plus 90 ns, in the nTOF window. The 90 ns is such that: the 30 ns is the estimated transit time in the PMT in the nTOF detector; and the 60 ns is the approximate time of flight for a DD neutron to the nTOF detector at 1.3 m. This means that the signal seen by the oscilloscope is delayed by both the cable length, and the PMT transit time. Using trapz(), the rest of the signal's amplitude is summed with respect to the dt of the time window's resolution. This is the assumed neutron signal area.

Cross Calibration of the Top and Bottom nTOFs

However, the two nTOFs cannot be compared without a cross-calibration. Because the bottom nTOF detector usually has a Pb puck of 1-inch thickness in front of it, a series of shots taken without the puck were analyzed to compare the signal areas of the top and bottom nTOFs in order to determine the ratio between the two when neither have any Pb shielding. 28 shots out of 41 taken were used for analysis. Based on those shots, it appears that the average ratio of neutron signal area of the Top to Bottom nTOF is 3.11 ± 0.81.

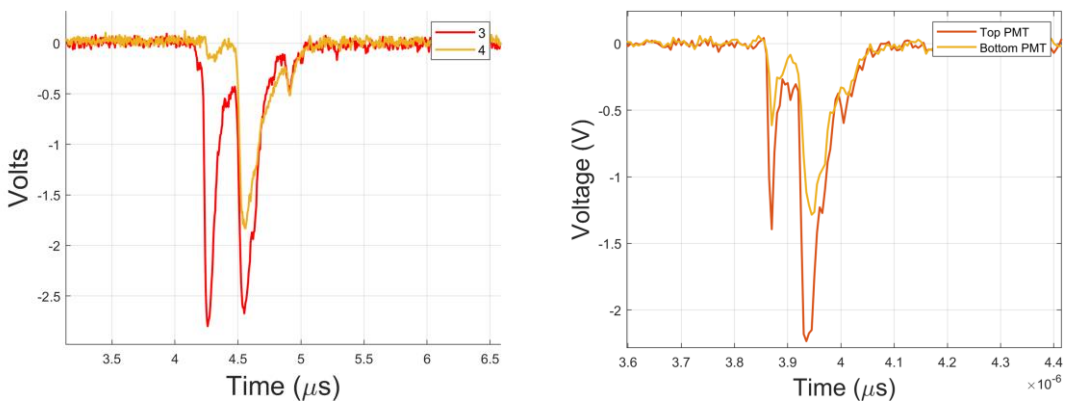

Figure 11. An example of one shielded and one unshielded nTOF (left) and two unshielded nTOF detectors (right).

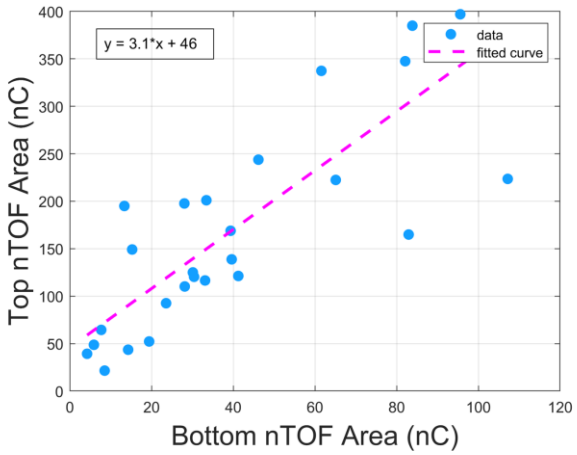

Figure 12. Plotted above are the Top nTOF neutron areas versus the Bottom nTOF neutron areas and the calculated linear fit.

Calibrating nTOF Signal Area to Neutron Yield

Finally, we make the fit of the area data to neutron yield using a polynomial of order 1 with an intercept of (0,0), corresponding to zero Coulombs at zero neutron yield. Hence, the fits for all data above the LDL generate: 1.12 ± 0.20 nC /n for the Top nTOF; and 0.23 ± 0.03 nC/n for the Bottom nTOF.

Table 2. Fit data for the Top and Bottom nTOFs.

	Top nTOF	Bottom nTOF
Above LDL (nC/n)	1.12 ± 0.20	0.23 ± 0.03
Photons/2.45 MeV neutron	8100 ± 1500	1700 ± 220

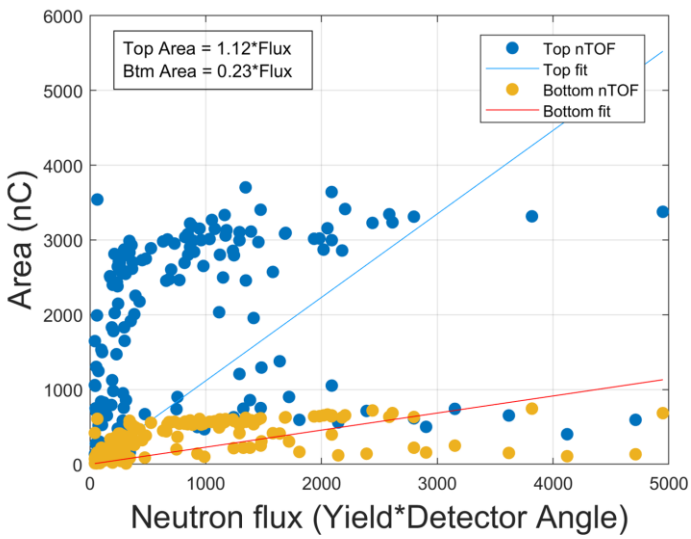

Figure 13. A scatter plot of all Top and Bottom nTOF areas tabulated versus corresponding neutron count at the solid angle subtended by each detector.

Given the fit data in Table 2 and using the efficiencies in Table 1, we can estimate the efficiencies of both nTOF detectors. Based on the first fit calculation using all data above the LDL threshold of the Be-activation detector, and with a photocathode conversion efficiency of

26% for the PMT plus a gain of $3.3 \cdot 10^6$, we can find the initial number of scintillation photons that originally impinged on the PMT for each nTOF detector.

Using all data, the scintillation efficiencies calculated from fitting nTOF signal area to neutron yield as seen at the detector are 8100 and 1700 photons/2.45 MeV n, for the Top and Bottom nTOFs respectively. LaPlace's work [14] on calibrating EJ-204 scintillators to determine the relative light yields (RLYs) for lower-energy proton recoil spectra suggests, if all RLYs in Table A.3 are simply averaged, that the proton light yield for impact by a fast neutron is about 0.56·10,400 photons, or, about 5800 photons.

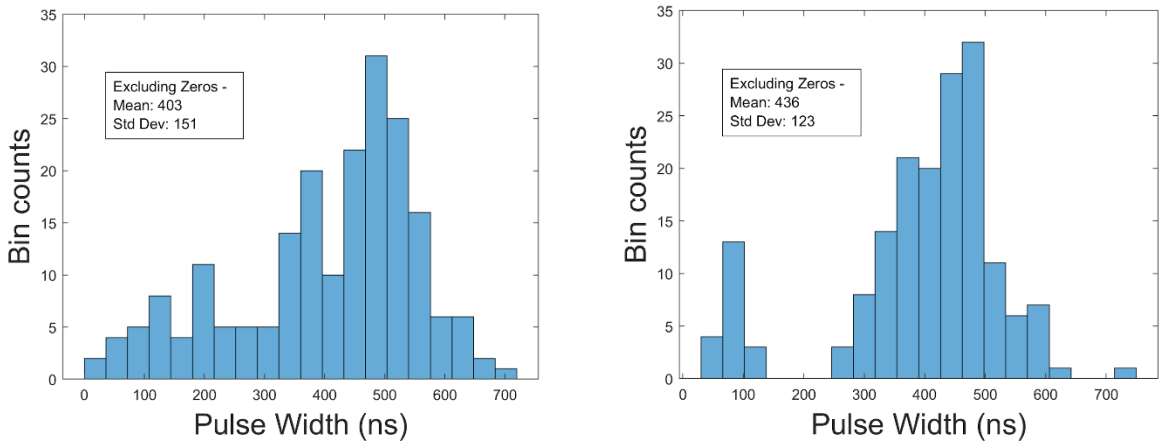

Figure 14. Averaged pulse widths (ns) in bin counts. Top nTOF pulse widths are on the left, and Bottom nTOF pulse widths are on the right.

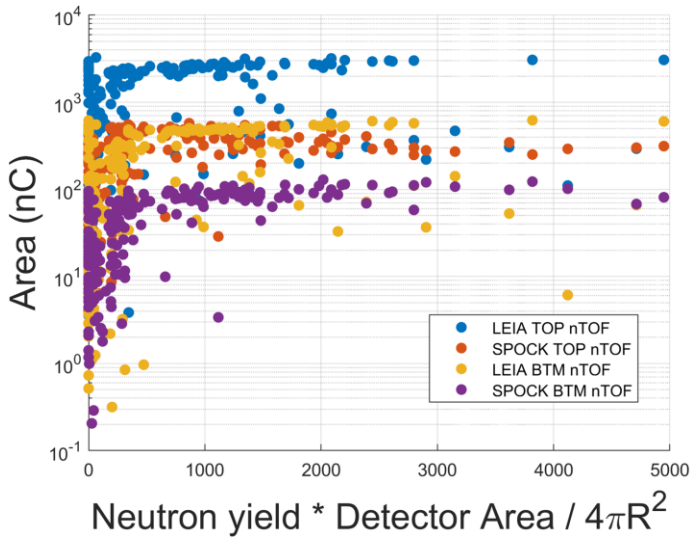

Figure 15. The areas plotted by oscilloscope and Top or Bottom nTOF detector. Though the signal voltage for each detector was presumably divided evenly, this figure clearly shows that a consistent discrepancy existed between the signals on both oscilloscopes.

The histograms in Figure 14 show distributions of the pulse widths (taken at 10% of maximum peak amplitude in a given waveform) of all the data for both the Top and Bottom nTOFs. Pulse width was averaged across the nTOF data from both oscilloscopes. Notably, the average width appears to be on the order of a few hundred nanoseconds. Secondary scattering of DD neutrons by fixtures external to the DPF chamber could explain this extended length, especially given that the decay time of a scintillator is generally only a few nanoseconds.

In Figure 15, signal areas are plotted versus neutron flux separated by oscilloscope (LEIA/SPOCK) and nTOF detector (Top/Bottom). It appears that for each nTOF detector, the difference between oscilloscopes comes out to a factor of 5 to 6. This does not represent an even voltage division of each signal, though that was assumed in the analysis. It is possible then that the voltage division is definitely uneven due to an unknown factor(s). Further work could include inspecting the apparatus that performs the voltage division for any defects, and then modify the analysis correspondingly to generate a more accurate fit of yield to neutron flux.

Furthermore, because contributions of area from the scintillator and PMT rise and decay components, these preliminary fits are likely overestimates. As such, further analysis must deconvolve these contributions from each waveform to make the fit more accurate.

DISCUSSION AND FUTURE WORK

Given the results and analysis, we find that the nTOF detectors examined within the scope of this thesis have scintillation efficiencies of an estimated 8100 and 1700 photons per 2.45 MeV neutron for the Top and Bottom nTOFs, respectively, for all data above the LDL of the Be activation detector. Dark current is not taken into consideration for this analysis, and the areas contributed by the decay and transit times of the EJ-204 and Hamamatsu R7724 are included with neutron area in the analysis, not deconvolved and subtracted. One 2.45 MeV neutron correlates with 1.12 nC and 0.23 nC on the Top and Bottom nTOF detectors, respectively.

This author highly recommends that future work tabulates the nTOF signal areas manually in addition to this automated analysis, to possibly refine and improve the variances in the data. The area contributions from the scintillator and PMT should also be deconvolved from each signal area. Additionally, this author also recommends that future data should be collected on one oscilloscope for a sufficient number of DPF shots, and have the same analysis be conducted on that data set separately to see if the discrepancy in signal area disappears or remains between each oscilloscope.

Additionally, a more accurate comparison of the sensitivities of the top and bottom nTOF detectors could include many more shots without any Pb shielding for the cross-calibration. The two detectors could also be switched in position to account for any variation in yield detection based on height. Simulations in could be performed to analyze the approximate proton recoil energy spectra that correlate with the neutrons generated on this particular DPF.

To improve the physical understanding of the type of DD neutron generation in the UCSD DPF, one could calibrate an axial PMT nTOF using a similar methodology. Additionally, an nTOF with a narrower energy resolution could be developed and fielded with an SiPM, or, silicon photomultiplier.

REFERENCES

[1] Francis F. Chen, *Introduction to Plasma Physics and Controlled Fusion*, 3rd Ed. Springer, 2016.

[2] Dwight R. Nicholson, *Introduction to Plasma Theory*. John Wiley & Sons, 1983.

[3] National Research Council, Committee on High Energy Density Plasma Physics. *Frontiers in High Energy Density Science: The X-Games of Contemporary Science*. 2003.

[4] M. Krishnan, "The Dense Plasma Focus: A Versatile Dense Pinch for Diverse Applications." IEEE Transactions on Plasma Science, Vol. 40, No. 12, Dec. 2012.

[5] V. Fillipov, T.I. Fillipova, and V.P. Vinogradov, "Dense high-temperature plasma in a non-cylindrical Z-pinch compression," Nucl. Fusion Suppl., vol. 2, pp. 577–587, Jan. 1962.

[6] J.W. Mather, "Investigation of the high-energy acceleration mode in the coaxial gun," Phys. Fluids Suppl., vol. 7, no. 11, pp. S28–S34, Nov. 1964

[7] B. Appelbe and J. Chittenden. "Neutron spectra from beam-target interactions in dense z-pinches." *Physics of Plasmas* **22**, 102703 (2015).

[8] PMT schematic: By Qwerty123uiop, CC BY-SA 3.0, https://commons.wikimedia.org/w/index.php?curid=62426194

[9] J. Birks, *The Theory and Practice of Scintillation Counting*. Pergamon, 1964.

[10] D. Housley, E.N. Hahn, J. Narkis, J.R. Angus, A.J. Link, F. Conti, and F.N. Beg. "Effect of insulator surface conditioning on the pinch dynamics and x-ray production of a Ne-filled dense plasma focus." *Journal of Applied Physics* **129**, 223303 (2021).

[11] C.L. Ruiz, R.J. Leeper, F.A. Schmidlapp, G. Cooper, and D.J. Malbrough. "Absolute calibration of a total yield indium activation detector for DD and DT neutrons." *Review of Scientific Instruments* **63**, 4889 (1992).

[12] G.F. Knoll, *Radiation Detection and Measurement*, 3rd Ed. John Wiley & Sons, 2000.

[13] E. N. Hahn, S. Ghosh, V. Eudave, J. Narkis, J. R. Angus, A. J. Link, F. Conti, F. N. Beg. "Effect of Insulator Length and Fill Pressure on Filamentation and Neutron Production in a 4.6 kJ Dense Plasma Focus." Manuscript.

[14] T.A. Laplace, B.L. Goldblum, J.A. Brown, D.L. Bleuel, C.A. Brand, G. Gabella, T. Jordan, C. Moore, N. Munshi, Z.W. Sweger, A. Ureche,

E. Brubaker. “Low Energy Light Yield of Fast Plastic Scintillators.” *Nuclear Inst. and Methods in Physics Research, A* (2018).

[15] V. Eudave. “Anode Shape and Structure Effects on Dense Plasma Focus Neutron Yield.” Thesis manuscript submitted for Master of Science, August 2022.